










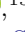





NICER observations of thermonuclear bursts from 4U 1728-34: Detection of oscillations prior to the onset of two bursts

Z. FUNDA BOSTANCI ^{1,2} TUĞBA BOZTEPE ³ TOLGA GÜVER ^{1,2} TOD E. STROHMAYER ⁴ YURI CAVECCHI ⁵
ERSIN GÖĞÜŞ ⁶ DIEGO ALTAMIRANO ⁷ PETER BULT ^{8,9} DEEPTO CHAKRABARTY ¹⁰ SEBASTIEN GUILLOT ¹¹
GAURAVA K. JAISAWAL ¹² CHRISTIAN MALACARIA ¹³ GIULIO C. MANCUSO ^{14,15} ANDREA SANNA ¹⁶ AND
JEAN H. SWANK ⁹

¹*Istanbul University, Science Faculty, Department of Astronomy and Space Sciences, Beyazıt, 34119, İstanbul, Türkiye*

²*Istanbul University Observatory Research and Application Center, Istanbul University 34119, İstanbul Türkiye*

³*Istanbul University, Graduate School of Sciences, Department of Astronomy and Space Sciences, Beyazıt, 34119, İstanbul, Türkiye*

⁴*Astrophysics Science Division and Joint Space-Science Institute, NASA's Goddard Space Flight Center, Greenbelt, MD 20771, USA*

⁵*Departament de Física, EEBE, Universitat Politècnica de Catalunya, Av. Eduard Maristany 16, 08019 Barcelona, Spain*

⁶*Faculty of Engineering and Natural Sciences, Sabancı University, Orhanlı-Tuzla 34956, İstanbul, Türkiye*

⁷*School of Physics and Astronomy, University of Southampton, Southampton, SO17 1BJ, UK*

⁸*Department of Astronomy, University of Maryland, College Park, MD 20742, USA*

⁹*Astrophysics Science Division, NASA Goddard Space Flight Center, Greenbelt, MD 20771, USA*

¹⁰*MIT Kavli Institute for Astrophysics and Space Research, Massachusetts Institute of Technology, Cambridge, MA 02139, USA*

¹¹*Institut de Recherche en Astrophysique et Planétologie, UPS-OMP, CNRS, CNES, 9 avenue du Colonel Roche, BP 44346, F-31028 Toulouse Cedex 4, France*

¹²*DTU Space, Technical University of Denmark, Elektrovej 327-328, DK-2800 Lyngby, Denmark*

¹³*International Space Science Institute, Hallerstrasse 6, 3012 Bern, Switzerland*

¹⁴*Instituto Argentino de Radioastronomía (CCT-La Plata, CONICET; CICIPBA), C.C. No. 5, 1894 Villa Elisa, Argentina*

¹⁵*Facultad de Ciencias Astronómicas y Geofísicas, Universidad Nacional de La Plata, Paseo del Bosque s/n, 1900 La Plata, Argentina*

¹⁶*Dipartimento di Fisica, Università degli Studi di Cagliari, SP Monserrato-Sestu km 0.7, Monserrato 09042, Italy*

Submitted to ApJ

ABSTRACT

We present temporal and time-resolved spectral analyses of all the thermonuclear X-ray bursts observed from the neutron star low-mass X-ray binary (LMXB) 4U 1728–34 with *NICER* from June 2017 to September 2019. In total, we detected 11 X-ray bursts from the source and performed time-resolved spectroscopy. Unlike some of the earlier results for other bursting sources from *NICER*, our spectral results indicate that the use of a scaling factor for the persistent emission is not statistically necessary. This is primarily a result of the strong interstellar absorption in the line of sight towards 4U 1728–34, which causes the count rates to be significantly lower at low energies. We also searched for burst oscillations and detected modulations in six different bursts at around the previously known burst oscillation frequency of 363 Hz. Finally, we report the detection of oscillations prior to two bursts at 356 and 359 Hz, respectively. This is the first time in the literature where burst oscillations are detected before the rapid rise in X-ray flux, from any known burster. These oscillations disappear as soon as the burst rise starts and occur at a somewhat lower frequency than the oscillations we detect during the bursts.

Keywords: stars: neutron – stars: oscillations – stars: accretion disks – X-rays: bursts – X-rays: binaries – X-rays: individual (4U 1728–34)

1. INTRODUCTION

Thermonuclear X-ray bursts (hereafter X-ray bursts) are flashes in X-rays, observed from numerous neutron star low-mass X-ray binary systems (Galloway et al.

2020). These flashes result from the unstable nuclear burning of the accreted material accumulated on the surface of the neutron star (Hansen & van Horn 1975; Lamb & Lamb 1978). During such an event, the ob-

served X-ray intensity increases by a factor of ~ 10 within $\sim 0.5 - 5$ s, and then decreases exponentially ($\sim 10 - 100$ s) as the surface of the star cools down. The energy released during a burst is typically $10^{39} - 10^{40}$ ergs. The peak flux, duration, evolution and other properties of the bursts depend on the chemical composition of matter and the proportion of material deposited per unit star surface area, hence on the accretion rate (Woosley et al. 2004). Since the amount of material deposited on the neutron star may evolve through different accretion rates for different bursts, in principle different burning regimes may be observed from the same source (see, e.g., Strohmayer & Bildsten 2006). The spectral and timing properties of X-ray bursts can be a useful tool for understanding neutron star parameters (such as radius, mass, and the equation of state, Bhattacharyya 2010; Özel et al. 2016; Özel & Freire 2016; Bogdanov et al. 2019). However, a comprehensive understanding of the interaction between burst emission and the surrounding environment is equally crucial for such studies. For example, recent findings from *NICER*, as well as some earlier results from *RXTE* (see, e.g., Worpel et al. 2013, 2015; Keek et al. 2018a,b; Bult et al. 2019; Buisson et al. 2020; Güver et al. 2022a,b; Bult et al. 2022), indicate that the persistent emission of a source may increase by up to an order of magnitude, especially around the peaks of the bursts. This excess emission is observed in the soft X-ray band (mostly below 3.0 keV), affecting the results obtained with instruments sensitive in the low energy bandpass. These findings are further supported by simulations showing an increase in the mass accretion rate onto the neutron star due to the combined effects of Poynting-Robertson drag, and reflection (Fragile et al. 2018, 2020; Speicher et al. 2022).

Nearly two decades after the first discovery of an X-ray burst from 4U 1728–34 (Hoffman et al. 1976), temporary oscillations during some of the bursts from this source were first discovered at 363 Hz by Strohmayer et al. (1996). Since then these burst oscillations have been firmly confirmed in approximately 20% of all known Type I X-ray bursters¹ (Watts 2012; Bilous & Watts 2019). The observed frequencies typically range from ~ 250 Hz to ~ 600 Hz, and they are attributed to the spin frequency of the neutron star. Burst oscillations are likely a result of rotational modulations caused by an asymmetric temperature distribution on the neutron star surface (Strohmayer et al. 1996, 1997; Chakrabarty et al. 2003). They are generally observed to occur at the rise/decay of some of the X-ray bursts (Watts et al.

2005; Watts 2012). Although the oscillation frequencies remain relatively consistent, there might be slight shifts of a few Hz during the typical duration of the burst, which lasts only a few seconds. Additionally, the oscillations occasionally vanish and then reappear throughout the burst (Muno et al. 2002a,b).

4U 1728–34 (a.k.a. the Slow Burster or MXB 1728–34) stands among the earliest discovered and most extensively studied bursting LMXBs. Its bursts were first explored by SAS-3 and Uhuru (Kellogg et al. 1971; Lewin et al. 1976). It is known for its regular X-ray bursts (see, e.g., Zhang et al. 2016; Kajava et al. 2017; Bhattacharyya et al. 2018) and burst oscillations (see, e.g., Strohmayer et al. 1996; van Straaten et al. 2001; Franco 2001; Verdhan Chauhan et al. 2017; Mahmoodifar et al. 2019), with a total of 96 bursts reported by Basinska et al. (1984a). According to the Multi-INstrument Burst ARchive (MINBAR², Galloway et al. 2020) a total of 1173 bursts have been detected with multiple instruments (RXTE/PCA, BeppoSAX/WFCs, INTEGRAL/JEMX), and no event with short recurrence has been reported. The source is thought to be an ultracompact X-ray binary (Shaposhnikov et al. 2003; Galloway et al. 2008) inferred from the burst behavior with a H-poor donor. However, Vincentelli et al. (2020) and Vincentelli et al. (2023) found that the orbital period of 4U 1728–34 must be greater than ~ 1.1 h or even ~ 3 h, based on infrared observations of the delay between X-ray bursts and its reflection off disc and companion. Such an estimate contradicts the proposed ultra-compact nature and suggests that the companion should be a helium star. The distance to the source is estimated to range from 4.4 to 5.1 kpc using Eddington limit estimations of the photospheric radius expansion bursts (Di Salvo et al. 2000; van Straaten et al. 2001; Galloway et al. 2003; Qiao & Liu 2019).

In this paper, we report the detection and the X-ray time-resolved spectral and temporal analysis of the bursts from 4U 1728–34, as observed with *NICER*. In total, we have identified 11 X-ray bursts in the archive, seven of which have previously been reported by Mahmoodifar et al. (2019). We detect burst oscillations in six of these events, three of which were also found by Mahmoodifar et al. (2019). Finally, we devote particular attention to two bursts that exhibited oscillations immediately before the observed increase in the count rate.

2. OBSERVATIONS AND DATA ANALYSIS

¹ <https://personal.sron.nl/~jeanz/bursterlist.html>

² <https://burst.sci.monash.edu/minbar/>

4U 1728–34 was observed with the *NICER* X-ray Telescope Instrument (XTI, Okajima et al. 2016; Gendreau et al. 2016) on board the International Space Station. The source was monitored from June 2017 to September 2019 for a total unfiltered and cleaned exposure of 230 ks and 163 ks, respectively. We used all public observations available through HEASARC³. These observations are gathered under ObsIDs starting with 0050150106, 1050150102 – 1050150158, and 2587010101 – 2587010104. We processed the data using *NICERDAS* v8c with *HEASoft* version v6.29c and used *ftool* XSELECT to extract light curves and spectra following the standard criteria of the *nicerl2*⁴ tool. We used the task *barycorr* to apply barycentric corrections for the analysis assuming the source coordinates (J2000) as $17^h 31^m 57.73^s$ and $-33^\circ 50' 02.5''$.

In order to identify X-ray bursts, we generated 0.25 s binned light curves in the 0.5–10 keV energy range and searched for the characteristic fast-rise exponential-decay features (Galloway et al. 2020). In total, we have identified 11 X-ray bursts across all the observations. The light curves of these bursts are shown in Figure A1, where BID denotes the burst number. Following Güver et al. (2022b) and using 0.5 s light curves including all the events in the 0.5–10 keV range, we defined the start time of a burst when the count rate is 4σ above the persistent rate (see Section 2.1). On the other hand, the rise time is defined as the interval between the burst start and the first moment when the count rate reached 98% of the burst’s peak value, which we label as the peak time. Regarding the decay phase of the bursts, we offer two definitions: the e-folding time is defined as the time when the count rate decreases by a factor of e after the peak moment, and the decay length is the time when the count rate decreases to 10% of the peak. The peak-rate, rise-time, pre-burst rate, e-folding time, and the decay time lengths of all bursts are listed in Table 1.

4U 1728–34 is classified as an atoll source based on the shape of the tracks in the color–color and hardness–intensity diagrams (Hasinger & van der Klis 1989). In order to determine the spectral state of the system when a burst was observed we constructed a hardness–intensity diagram. For this purpose, we generated light curves in the 0.5–2 and 4–10 keV bands with a time resolution of 128 s from clean event files (see, e.g., Güver et al. 2021, 2022a,b). The resulting hardness–intensity diagram is shown in Figure 1. Instances of X-ray bursts are indicated with red filled circles. From the hardness–

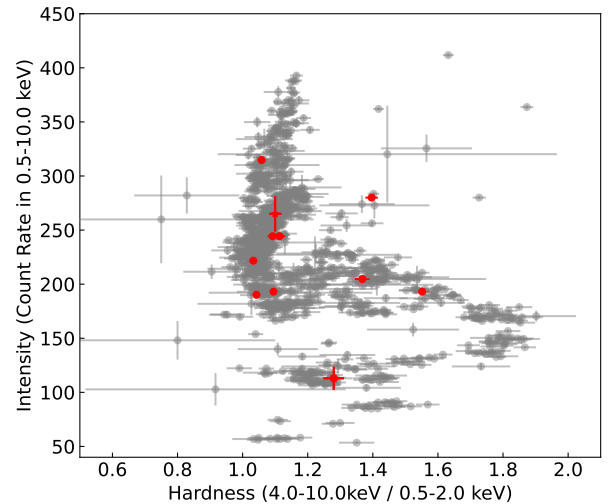


Figure 1. Hardness–Intensity diagram showing all *NICER* observations of 4U 1728–34 from 2017 to 2019. Observations in which an X-ray burst was detected are indicated by red filled circles.

intensity diagram, we see that the intensity primarily varies when the hardness is relatively low (~ 1.05) and bursts seem to happen when the hardness ratio is between 1.04 to 1.6. Notably, our observation dataset predominantly encompasses count rates $\gtrsim 220$ counts s^{-1} in the 0.5–10 keV range. On the other hand, during bursts 2 and 4, the intensity of 4U 1728–34 exhibits slight deviations with a count rate in the 0.5–10 keV of 331 counts s^{-1} and 112 counts s^{-1} , respectively.

Although the low orbit of *NICER* often prevents a conclusive analysis, we also examined the burst recurrence times, which is defined as the interval since the previous burst. Only for bursts 9 and 10 we can establish a limit on the recurrence as they both happen during the same observation. In that case, the recurrence time we measure is ~ 4.56 hours. Galloway et al. (2020) present the distribution of recurrence times for this source in the MINBAR catalog. The minimum recurrence observed from this source with RXTE/PCA is reported as 1.8 hours, while the maximum is 7.9 hours, with an average of 3.7 hours. The value we infer is compatible with this range although it remains slightly on the longer side of the distribution.

2.1. Time Resolved Spectral Analysis

The first step for the time-resolved spectral analysis is modeling the persistent emission of the source, since the persistent emission acts as a background during the burst. For that purpose we extracted a spectrum from the data obtained 100 s prior to each burst. In the case

³ <https://heasarc.gsfc.nasa.gov>

⁴ <https://heasarc.gsfc.nasa.gov/lheasoft/ftools/headas/nimaketime.html>

Table 1. Some characteristic properties of all thermonuclear X-ray bursts from 4U 1728–34 detected with *NICER*. Parameters are derived from 0.5–10 keV light curves with a time resolution of 0.5 s, therefore the uncertainties in the rise and decay times are 0.5 s. BID shows the observed burst number.

| BID | MJD (TDB) | OBSID | Peak-Rate ^a counts/s | Pre-burst Rate ^b counts/s | Rise-Time s | e-folding time s | Decay Time ^c s |
|-----|----------------|------------|------------------------------------|---|----------------|---------------------|------------------------------|
| 1 | 57940.82411458 | 0050150106 | 2265±71 | 223.3±1.6 | 1.75 | 5.5 | 15.0 |
| 2 | 57953.11721065 | 1050150102 | 2805±79 | 331.3±1.7 | 1.50 | 6.5 | 16.5 |
| 3 | 57979.45513310 | 1050150111 | 1857±65 | 220.8±1.6 | 1.50 | 5.5 | 14.5 |
| 4 | 57998.09995718 | 1050150127 | 2289±69 | 111.4±3.2 | 2.25 | 6.5 | 23.5 |
| 5 | 58006.66877199 | 1050150134 | 1999±67 | 243.1±1.7 | 1.75 | 5.5 | 17.0 |
| 6 | 58010.09684144 | 1050150137 | 4204±94 | 232.1±1.5 | 0.75 | 5.0 | – ^d |
| 7 | 58156.69664468 | 1050150149 | 2265±70 | 207.2±1.5 | 1.00 | 8.0 | 23.0 |
| 8 | 58308.89758681 | 1050150158 | 1921±65 | 203.5±1.4 | 1.00 | 10.5 | 21.5 |
| 9 | 58724.34034375 | 2587010101 | 2840±79 | 262.4±1.8 | 1.00 | 7.5 | 19.5 |
| 10 | 58724.53015278 | 2587010101 | 2022±67 | 240.1±6.7 | 1.00 | 9.0 | 36.0 |
| 11 | 58727.84581481 | 2587010104 | 2920±80 | 246.3±1.7 | 0.75 | 5.5 | 14.0 |

^a Pre-burst count rates are subtracted.

^b Calculated as the average count rate 100 s prior to the burst start time. Uncertainties reflect the standard error of the average of all the count rates used.

^c The time for the count rate to reach 10% of the peak value.

^d Good time interval (GTI) ended before reaching the criteria.

of burst 4 unfortunately there is only a 24 s interval available before or after the burst. We therefore used this data for estimating the persistent spectrum of the source before the burst. In the case of burst 10, the pre-burst data had only an exposure time of 30 s so we used postburst X-ray spectra as our background. In burst 5, overshoot⁵ rates are very high and show significant variations throughout the burst, which mostly affected our estimation of the energy distribution of the persistent emission. Therefore we did not include this burst in our spectral analysis (see, e.g., Bult et al. 2019; Güver et al. 2022b).

For each observation, we also generated background spectra using the `nibackgen3C50` tool (Remillard et al. 2022) as well as the response matrix files (RMFs) and ancillary response files (ARFs) using `nicerrmf` and `nicerarf`, respectively. We analyzed spectral data in the 1–10 keV range utilizing *Sherpa* (Freeman et al. 2001) with custom python scripts aided by Astropy (Astropy Collaboration et al. 2018), NumPy (Van Der Walt et al. 2011), Matplotlib (Hunter 2007), and Pandas (Wes McKinney 2010). Following Güver et al. (2021, 2022a,b), we tried several modeling options including thermal (blackbody and disk blackbody models) and non-thermal (power-law, Compton scattering models) components. The resulting fits indicate that the pre-burst spectra of 4U 1728–34 can often be modeled as-

suming a simple absorbed power-law component. For the interstellar absorption, we used the *tbabs* model (Wilms et al. 2000) assuming ISM abundances (Wilms et al. 2000) and cross-sections as presented by Verner & Yakovlev (1995). Initially, we allowed the hydrogen column density values to be free before each burst. We then calculated the error weighted average of all the best-fit values and used the resulting value, $N_{\text{H}} = 4.18 \times 10^{22} \text{ cm}^{-2}$, as a fixed parameter for further analysis. To determine the average Hydrogen column density we excluded the pre-burst data from burst 4, where the exposure time for that spectrum was much shorter. Our best-fit hydrogen column density is in agreement with Sleator et al. (2016); Mondal et al. (2017); Wang et al. (2019) who reported values in the range $N_{\text{H}} \sim 3.9 - 4.6 \times 10^{22} \text{ cm}^{-2}$. However, it is important to note that in most instances, the hydrogen column density towards 4U 1728–34 is found to be much lower i.e, $N_{\text{H}} \sim 2.6 - 2.9 \times 10^{22} \text{ cm}^{-2}$ (see, e.g., D’Ai et al. 2006; Wroblewski et al. 2008; Eggen et al. 2011; Worpel et al. 2013). We present the best-fit results of this analysis in Table 2 where we also provide the 1–10 keV unabsorbed fluxes using the `sample_flux` command within *sherpa*. The uncertainties in the fluxes are calculated by drawing 10000 samples from a normal distribution whose mean and the standard deviation equals the best fit parameter value and its 1σ uncertainty.

To track the spectral evolution throughout the bursts, we generated X-ray spectra following the methods outlined by Galloway et al. (2008); Güver et al. (2012b, 2021, 2022a,b) by adaptively determining the exposure

⁵ https://heasarc.gsfc.nasa.gov/docs/nicer/analysis_threads/overshoot-intro/

Table 2. Best fit model results for pre-burst X-ray spectra of 4U 1728–34 using a single power-law model. γ values are also provided assuming an Eddington limit of $4.04 \times 10^{-8} \text{ erg s}^{-1} \text{ cm}^{-2}$ as described in subsection 3.1.

| BID | Γ | Flux* | χ^2 / dof | γ |
|-----|-----------|-----------|-----------------------|----------|
| 1 | 1.52±0.02 | 3.61±0.11 | 478.44/332 | 0.09 |
| 2 | 1.86±0.01 | 4.85±0.11 | 381.17/389 | 0.12 |
| 3 | 1.49±0.02 | 3.48±0.10 | 312.01/326 | 0.09 |
| 4 | 1.80±0.08 | 0.67±0.01 | 11.54/18 | 0.02 |
| 6 | 1.86±0.02 | 3.39±0.09 | 341.23/323 | 0.08 |
| 7 | 1.71±0.02 | 3.12±0.09 | 328.59/302 | 0.08 |
| 8 | 1.83±0.02 | 2.98±0.09 | 313.32/290 | 0.07 |
| 9 | 1.81±0.01 | 3.88±0.10 | 378.87/357 | 0.10 |
| 10 | 1.85±0.01 | 4.13±0.10 | 450.21/362 | 0.10 |
| 11 | 1.81±0.02 | 3.84±0.10 | 315.86/342 | 0.95 |

* Unabsorbed 1–10 keV flux in units of $\times 10^{-9} \text{ erg s}^{-1} \text{ cm}^{-2}$.
Note : We fixed the $N_{\text{H}} = 4.18 \times 10^{22} \text{ cm}^{-2}$.

time. We started our exposure times for each spectrum from 0.125 s and increased following the change in the observed count rates, to be able to keep the uncertainty in the inferred spectral parameters as comparable as possible. A typical average count rate is ~ 560 counts/s. For each X-ray spectrum, we initially used the best-fit model with fixed parameters for the persistent emission and subtracted only the background generated by the *nibackgen3C50* tool. If statistically required, we then added a blackbody component to account for the additional emission from the X-ray burst and followed its spectral evolution. We also calculated the bolometric X-ray flux of the blackbody component using the *sample_flux* command within *sherpa* in the 0.01 – 200 keV range for each modeled burst spectrum. In addition to this approach, we also tried to add a scaling factor, f_a (following Worpel et al. 2013, 2015; Güver et al. 2022a,b), to the persistent emission model. However, as shown in Section 3.1, contrary to previous findings from *NICER*, in the case of 4U 1728–34 this approach did not yield statistically significant improvements for most spectra.

2.2. Search for Burst Oscillations

We performed a timing analysis based on Z_n^2 statistics to search for burst oscillations across 11 bursts. The Z^2 statistic is defined as follows:

$$Z_n^2 = \frac{2}{N_\gamma} \sum_{k=1}^n \left[\left(\sum_{j=1}^{N_\gamma} \cos k\nu t_j \right)^2 + \left(\sum_{j=1}^{N_\gamma} \sin k\nu t_j \right)^2 \right], \quad (1)$$

where Z^2 represents the measured power of the signal, n is the number of harmonics ($k = 1 \dots n$ is the index), N_γ is the number of photons used in the time bin, ν denotes the frequency under consideration, and t_j is the arrival time of the j th count relative to some reference time. In the absence of a coherent signal Z_n^2 powers follow a χ^2 distribution with $2n$ degrees of freedom (Buccheri et al. 1983).

We selected $n = 1$ for our search. We constructed dynamical power spectra using search intervals of 2 s and 4 s. These time windows are then shifted with a step size of 1/32 s. Since the reported signals for burst oscillations in 4U 1728–34 range between 358 and 367 Hz according to Galloway et al. (2020), we considered frequencies between 355 and 370 Hz with a frequency step of 0.1 Hz. We searched for burst oscillations in three different energy bands, 0.5–12, 0.5–6, and 6–12 keV in order to compare our results with those of Mahmoodifar et al. (2019). We identify signals with the highest powers and then computed the probability of the signals assuming a Poisson noise distributed as χ^2 with two degrees of freedom.

We also computed the fractional rms amplitude of candidate oscillations in each burst from phase-folded light curves obtained in the time interval of the light curve in which the signal is significant. Then we fitted the phase-folded light curves with a sinusoidal model defined as $A + B \sin(2\pi\nu t - \phi_0)$, and from the best fitting parameters we calculated the fractional rms defined as $B/(\sqrt{2}A)$ (see, e.g., Bilous & Watts 2019).

3. RESULTS & DISCUSSION

Below we present the main findings of our analysis on the spectral and temporal properties of the detected thermonuclear bursts from 4U 1728–34.

3.1. Spectral Results

We present the resulting best fit parameters for the persistent emission preceding the detected bursts in Table 2. In Figure 2 and 3 we present the observed spectral evolution in each burst. The inferred best fit parameters at the peak flux moment along with the fluences of each burst are summarized in Table 3. In the calculation of the fluence, we integrated the bolometric fluxes starting from the onset of a burst till it declines to 10% of the peak flux. Contrary to the earlier findings from *NICER* (see, e.g., Keek et al. 2018a,b; Bult et al. 2019; Buisson et al. 2020; Güver et al. 2022a,b; Bult et al. 2022), the spectral results reveal that in the case of 4U 1728–34 the multiplication of the persistent emission with a scaling factor does not improve the fits. In most cases this is because the fits are already statistically acceptable when

we just use the persistent emission as a fixed model plus a blackbody for the burst emission, as shown in Figure 4. In rare cases, only about 2% of the total spectra within the flux limits, the application of a scaling factor is statistically favorable (f-test yields a chance probability smaller than 5%). However, in these cases we see that the reduced χ^2 values are mostly below unity indicating an overfitting issue. A simple explanation of this issue may be related to the fact that we use only the 1–10 keV band as opposed to most of the earlier studies where the authors used 0.5–10 keV range. We tested this by running our fits in the 0.5–10 keV range as well. We saw that in this case the fraction of X-ray spectra where the addition of the f_a improves the fit increases to 9% of the total. However, this is still much smaller compared for example to 4U 1636–536 where in 63% of the spectra a scaling factor is needed (Güver et al. 2022b). This discrepancy may be attributed, in part, to the substantial hydrogen column density inferred along

the line of sight towards 4U 1728–34 $N_{\text{H}} = 4.18 \times 10^{22}$. Similarly, Güver et al. (2021) and Bult et al. (2021) also found that a scaling factor is not necessary for 4U 1608–52 and XTE J1739–285. In both cases the hydrogen column densities in the line of sight to these sources were significantly high with $N_{\text{H}} = 1.4 \times 10^{22}$ and $N_{\text{H}} = 1.73 \times 10^{22}$, for 4U 1608–52 and XTE J1739–285, respectively (Güver et al. 2021; Bult et al. 2021). These findings further confirm that the excess emission detected during X-ray bursts is mostly observed in the soft X-ray band, below 2.5 keV, irrespective of the observed low mass X-ray binary and does not really contribute significantly in the 3–10 keV band.

In Figure 5, we compare our spectral parameters obtained at the peaks of each burst with those from the MINBAR catalog (Galloway et al. 2020), which includes 611 bursts detected from 4U 1728–34. Our results seem to be in very good agreement with the range obtained from the MINBAR sample.

Table 3. Spectral parameters obtained at the peak flux moment for each burst. The fluence of each burst is also presented.

| BID | Peak Flux ^a | Peak kT | Peak Radius ^b | Fluence ^c | PRE ^d |
|-----|------------------------|-----------|--------------------------|----------------------|------------------|
| | | (keV) | (km) | | |
| 1 | 9.81±2.43 | 3.74±0.71 | 4.16±0.69 | 36.8±1.43 | Y |
| 2 | 8.82±1.87 | 2.79±0.40 | 6.54±0.96 | 46.6±1.13 | M |
| 3 | 10.83±2.35 | 3.55±0.57 | 4.72±0.67 | 32.3±1.41 | N |
| 4 | 10.10±1.58 | 3.18±0.34 | 5.45±0.55 | 46.5±1.68 | M |
| 6 | 9.40±1.82 | 3.23±0.45 | 5.16±0.67 | 55.4±1.17 | Y |
| 7 | 7.24±0.96 | 2.38±0.20 | 7.89±0.75 | 29.4±0.85 | N |
| 8 | 6.01±0.89 | 2.34±0.20 | 7.39±0.72 | 28.7±0.75 | N |
| 9 | 9.89±2.21 | 2.83±0.44 | 6.77±1.05 | 38.6±0.97 | M |
| 10 | 7.21±1.15 | 2.71±0.28 | 6.15±0.71 | 30.9±0.97 | Y |
| 11 | 9.47±1.01 | 2.27±0.16 | 9.86±0.77 | 38.2±0.97 | M |

^aUnabsorbed bolometric flux in units of $\times 10^{-8}$ erg s⁻¹ cm⁻².

^bApparent blackbody radius assuming a distance of 5.31 kpc.

^cIn units of $\times 10^{-8}$ erg cm⁻².

^dThe “PRE” column indicates whether the burst exhibited a photospheric radius expansion (Y) or not (N), or whether this is not clear (M).

As shown by Galloway et al. (2008); Güver et al. (2012a); Galloway et al. (2020) 4U 1728–34 is one of the rare sources, together with 4U 1820-30 and 4U 1636-536, which show frequent photospheric radius expansion

bursts. The combined effects of high hydrogen column density towards 4U 1728–34 which decreases the observed count rate in the *NICER* band and the fast evolution of the bursts limit our capability to infer much from the spectral analysis. However, following the criteria proposed by Galloway et al. (2008) and Güver et al.

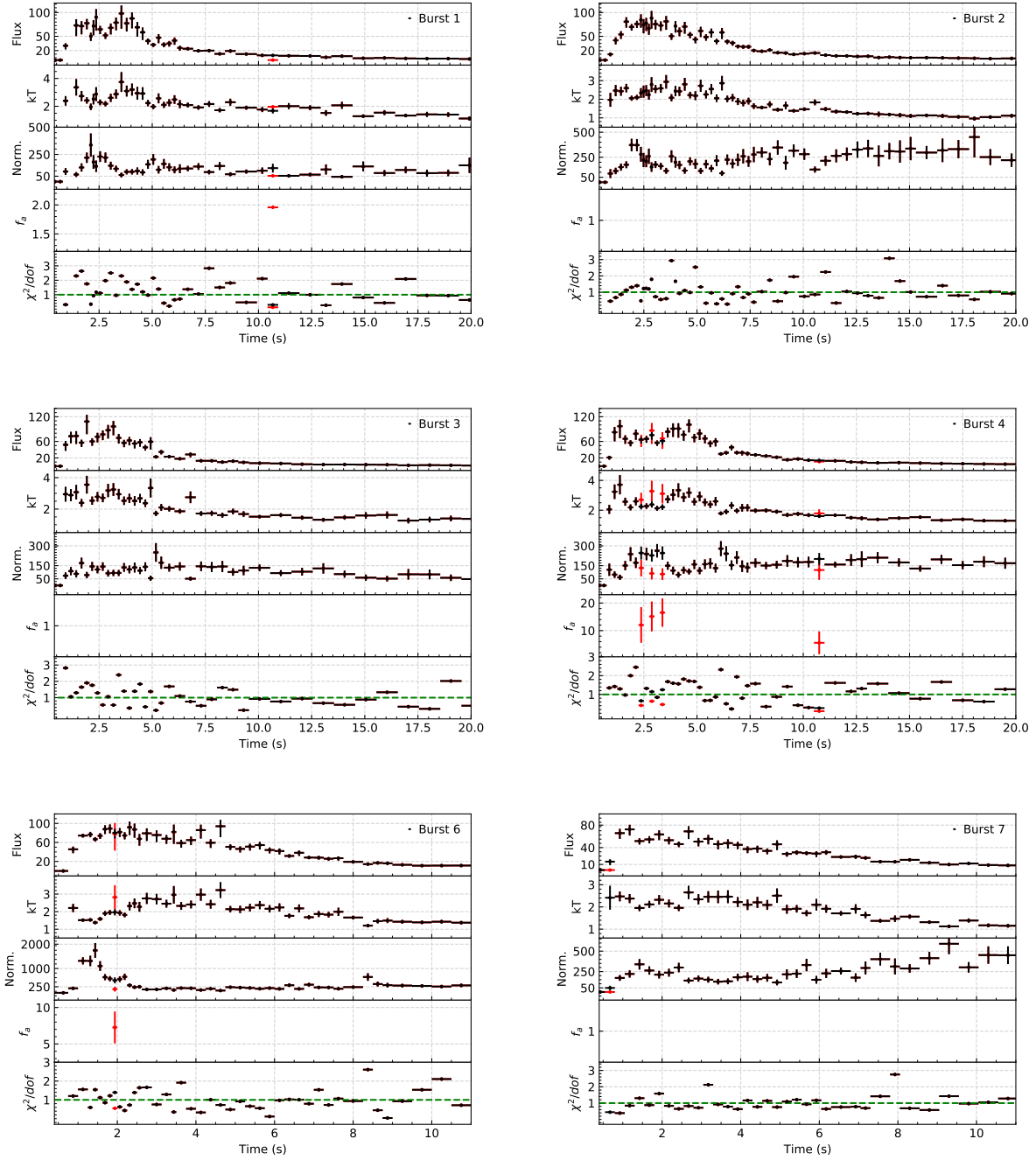


Figure 2. Time evolution of spectral parameters are shown. Red symbols show the results of the f_a method when applicable and black symbols show the results for constant background emission. In each panel, we show, from top to bottom, bolometric flux (in units of $10^{-9} \text{ erg s}^{-1} \text{ cm}^{-2}$), temperature (keV), blackbody normalization ($R_{\text{km}}^2/D_{10\text{kpc}}^2$), f_a , and finally the fit statistic, respectively.

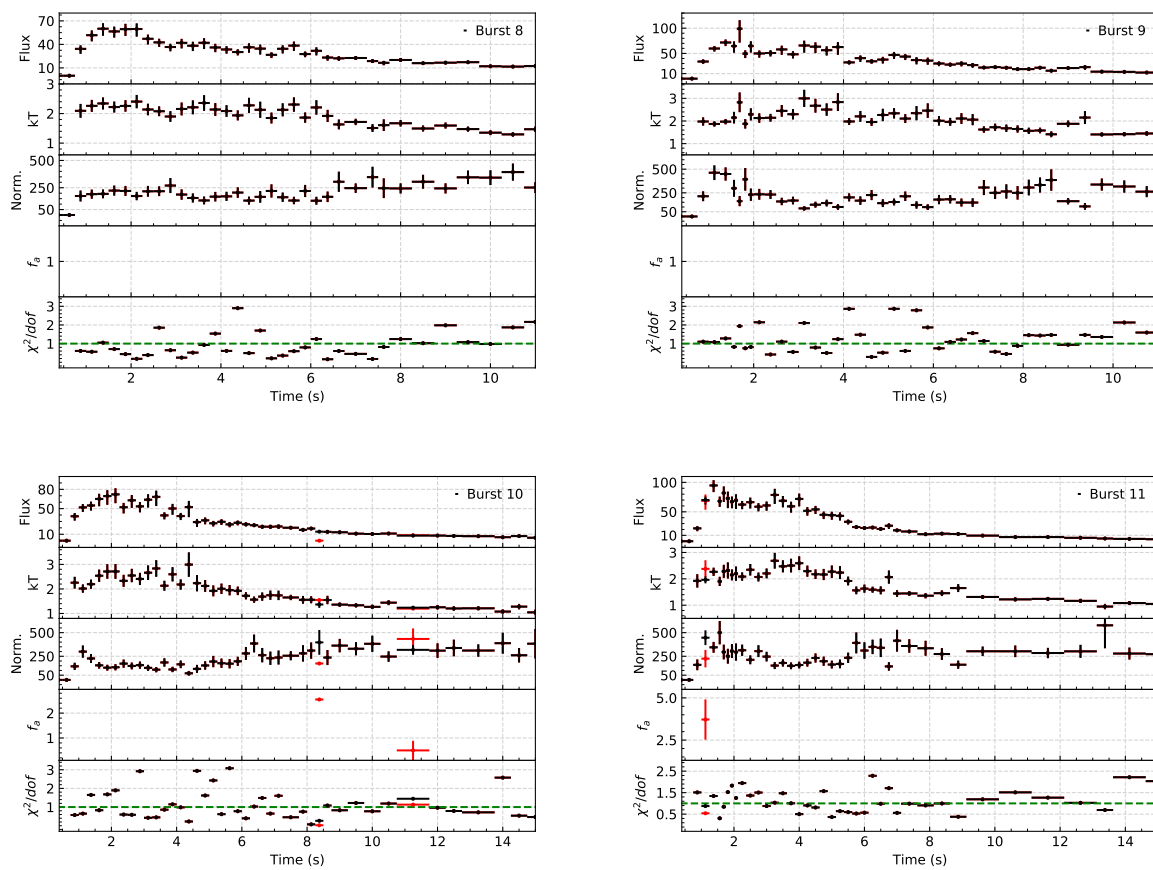


Figure 3. Same as Figure 2.

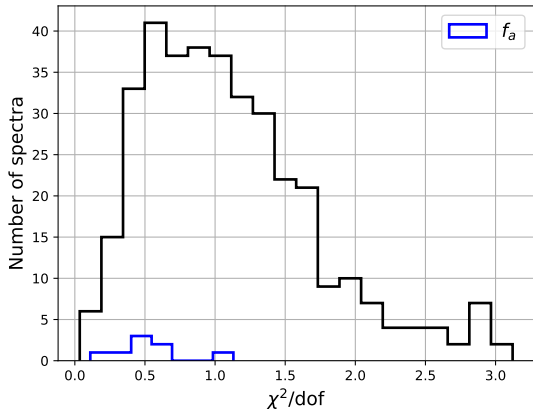


Figure 4. Histogram of the χ^2 values with or without the application of the f_a parameter. Only in a very small fraction of the cases the use of f_a is statistically required.

(2012a), we identified three bursts that show evidence for photospheric radius expansion and three more candidates. These bursts are indicated in Table 3. In Figure 6 we compare the touchdown fluxes and peak fluxes of the bursts as inferred with *NICER* with the touchdown flux value inferred using 16 bursts by Güver et al. (2012a). Although with much larger error bars, our results remain consistent with previous results. Note that the average peak flux for 4U 1728–34 reported as $F_{peak} = (9.4 \pm 3.6) \times 10^{-8} \text{ erg s}^{-1} \text{ cm}^{-2}$ in MINBAR (Galloway et al. 2020), also aligns well with the peak flux measurements presented in this study.

Photospheric radius expansion bursts can be used to infer the Eddington Limits (see, e.g., van Paradijs 1979; Damen et al. 1990; Özel & Freire 2016), as well as calculating the distances (Basinska et al. 1984b; Kuulkers et al. 2003). In order to calculate a distance for 4U 1728–34, we took the weighted average of the touchdown fluxes of bursts 1, 6 and 10 showing photospheric radius expansion $F_{TD} = (7.88^{+1.18}_{-0.70}) \times 10^{-8} \text{ erg s}^{-1} \text{ cm}^{-2}$. Using the observed flux value and assuming 10 km and $1.4 M_{\odot}$ for the radius and the mass of the neutron star as well as taking into account that the accreted matter can be hydrogen-rich ($X=0.7$) or hydrogen-poor ($X=0$), we estimate the distance as $d_H = 4.09^{+0.34}_{-0.17} \text{ kpc}$, $d_{He} = 5.31^{+0.45}_{-0.22} \text{ kpc}$, respectively. These values are in very good agreement with the distance estimations presented in (Galloway et al. 2008; Shaposhnikov et al. 2003) for 4U 1728–34.

In Table 3 we presented apparent emitting radii of the blackbody at the peak of each burst for a distance of 5.31 kpc, assuming 4U 1728–34 is accreting pure-He. Considering the burst timescales inferred in this study and in Galloway et al. (2008, 2020) it is a fair assump-

tion that 4U 1728–34 is a pure He accretor (Shaposhnikov et al. 2003) and may be an ultracompact binary. We note however that recent simultaneous infrared and X-ray observations support that the companion is a helium star, not an ultra-compact (Vincentelli et al. 2020, 2023).

Finally, using the touchdown flux derived above one can also calculate the γ value (van Paradijs et al. 1988; Galloway et al. 2008), which is defined as the ratio of the persistent bolometric flux to the Eddington limit (derived from the touchdown or peak fluxes of the bursts) of a source and is expected to be related to the mass accretion rate. Due to the nature of the power-law model we used to fit the persistent emission, it is not reliable to calculate unabsorbed bolometric flux of the source by just extrapolating the function with the best fit parameters. We therefore calculated the unabsorbed touchdown flux of the source limiting to only 1–10 keV range as in the persistent flux measurements. This way we find $F_{TD} = (4.04^{+0.2}_{-0.30}) \times 10^{-8} \text{ erg s}^{-1} \text{ cm}^{-2}$ in the 1–10 keV. We used this value and the persistent state fluxes of the source to calculate the γ values and present them in Table 2. We here made the assumption that in the persistent emission there is no additional contribution from the accretion disc below or above the 1–10 keV range that would significantly change the ratio. Overall the inferred γ values (see Table 2) show that during *NICER* observations the system was at about 10% Eddington, with the exception of bursts 4 and 8.

3.2. Timing Analysis and Detected Burst Oscillations

We consider signals as candidates when a single-trial chance probability is calculated to be $< 10^{-4}$ and a confidence level $> 99.7\%$ is reached in either one of the 2 or 4 s search intervals. With these criteria we identified candidate burst oscillation signals in 8 of the 11 bursts. All of the bursts and the resulting Z_1^2 contours are shown in Figure A1. Properties of these signals are listed in Table 4, including the energy range in which the signal is detected, frequency, power of the signal, single-trial chance probability, confidence level, fractional rms amplitude, the time it is detected with respect to the burst peak and finally the search window in which the signal is found. In our list, three candidate signals observed from bursts 4, 7, and 8 were also reported by Mahmoodifar et al. (2019), where the authors searched for oscillations in seven bursts covering the 360 and 365 Hz frequency range. Our findings for these three bursts are in agreement with the results presented in Mahmoodifar et al. (2019). Since the frequency range and the time interval we considered are wider, we found more candidate signals in the first seven bursts.

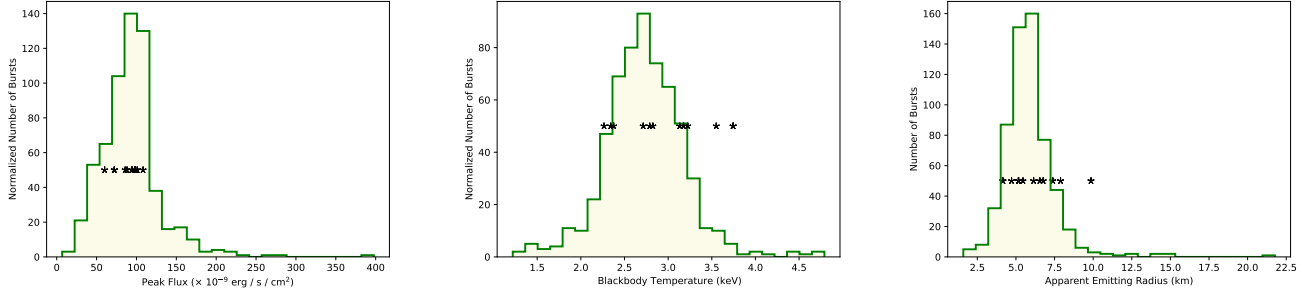


Figure 5. Histograms of peak flux, blackbody temperature and blackbody radius values assuming a source distance of 5.31 kpc in the MINBAR catalog together with the same values measured with *NICER* for 10 bursts (black stars) reported here.

Table 4. Characteristic properties of all the candidate burst oscillations. The values shown in bold indicate the search interval where the signal is more significantly detected.

| BID | Energy Range keV | Freq. Hz | Z_1^2 | Single Trial. | Conf. Level % | A_{rms} % | Time ^a s | Window Size s |
|----------------|---------------------|-------------|---------|----------------------|------------------|-----------------|------------------------|------------------|
| 1 | 0.5–12 ^b | 356.1 | 30.50 | 2.0×10^{-7} | 99.996 | 26.4 ± 3.3 | -2.31 | 2 |
| 3 | 0.5–6 ^c | 363.2 | 25.64 | 2.1×10^{-6} | 99.960 | 9.7 ± 1.4 | 2.35 | 2, 4 |
| 3 | 0.5–6 ^b | 367.0 | 23.01 | 1.0×10^{-5} | 99.849 | 15.5 ± 2.3 | -4.27 | 4 |
| 4 | 0.5–6 ^c | 367.5 | 23.77 | 6.9×10^{-6} | 99.897 | 19.9 ± 3.2 | 25.29 | 2, 4 |
| 4 ^d | 6–12 | 362.5 | 30.48 | 2.0×10^{-7} | 99.996 | 40.1 ± 5.8 | 7.66 | 2, 4 |
| 5 | 0.5–12 ^b | 355.5 | 24.22 | 5.5×10^{-6} | 99.918 | 13.0 ± 1.9 | 9.23 | 2, 4 |
| 7 ^d | 0.5–12 ^c | 363.1 | 28.09 | 8.0×10^{-7} | 99.988 | 9.2 ± 1.3 | 3.97 | 2, 4 |
| 8 ^d | 6–12 | 363.6 | 30.75 | 2.0×10^{-7} | 99.996 | 45.7 ± 6.7 | 13.45 | 2, 4 |
| 10 | 0.5–12 ^b | 357.9 | 21.87 | 1.7×10^{-5} | 99.733 | 11.0 ± 1.6 | 9.31 | 2, 4 |
| 10 | 6–12 | 359.0 | 27.62 | 1.0×10^{-6} | 99.985 | 63.7 ± 10.7 | -1.28 | 2, 4 |
| 11 | 0.5–12 ^b | 366.4 | 28.34 | 7.0×10^{-7} | 99.989 | 7.6 ± 1.0 | 1.80 | 2, 4 |

^aTime is given with respect to the peak moment of each burst.

^bAlso detected in 0.5–6 keV band.

^cAlso detected in 0.5–12 keV band.

^dAlready reported in [Mahmoodifar et al. \(2019\)](#).

In three bursts (3, 7 and 11) we detected candidate oscillations from the peaks to the e-folding times, in both 0.5–6 and 0.5–12 keV bands, as well as in both 2 and 4 s search interval windows. Bursts 3 and 7 show signals at around 363 Hz while during burst 11 an oscillation at 366 Hz is observed, which is well beyond our uncertainty in frequency (0.1 Hz). As seen in Table 4, the fractional rms amplitudes of these oscillations are in the range of 7 to 10%, which are consistent with burst oscillation rms amplitudes around peaks reported in previous studies ([Strohmayer et al. 1997](#); [van Straaten et al. 2001](#); [Mah-](#)

[moodifar et al. 2019](#)). Errors in rms amplitudes show 1σ confidence levels and are calculated from the best-fit parameters and their associated statistical uncertainties.

Bursts 4, 5, 8 and 10 show oscillations during the burst tail. In bursts 5 and 10, we detected signals at frequencies of 355.5 and 357.9 Hz in both 0.5–6 and 0.5–12 keV and in both 2 and 4 s search interval windows with maximum Z^2 values of 22 and 24, respectively. The fractional rms amplitudes for these oscillations range from 11–13% in the 0.5–6 and 0.5–12 keV bands. For bursts 4 and 8, we found signals around 363 Hz with the maximum power of just over 30 in the 6–12 keV band. The fractional rms amplitude of the signals in 6–12 keV band

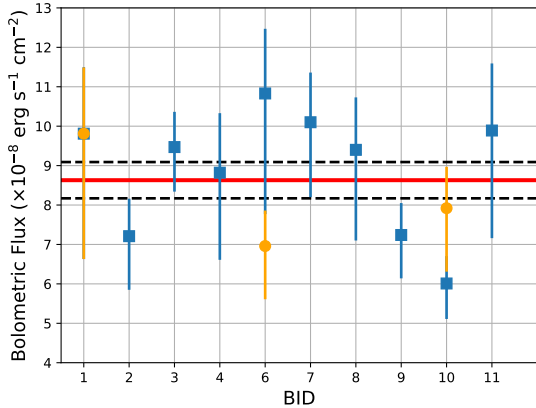


Figure 6. Touchdown (orange dots) and/or peak flux (blue squares) values measured here compared with the average touchdown flux value presented by Güver et al. (2012a), which is shown with the red solid line together with the systematic uncertainties shown with black dashed lines.

is very large, over 40%. Our finding of these two bursts is consistent with the results reported by Mahmoodifar et al. (2019). We also noticed a tentative signal at 367.5 Hz after the decay time of burst 4. This signal is observed in both 0.5–6 and 0.5–12 keV bands and in both 2 and 4 s search interval windows with an rms amplitude of about $20\% \pm 3\%$ (see, Table 4).

There are three bursts (1, 3, and 10) that deserve particular attention. As it can be seen in Table 4 and Figure A1 oscillations are observed just prior to the X-ray bursts and they fade away when bursts start to rise. In the case of burst 1, the signal at 356 Hz is detected in 0.5–6 and 0.5–12 keV bands with an rms amplitude of about $26\% \pm 3\%$. The oscillation seems to reach a maximum Z^2 of slightly over 30 just 2.3 ± 1.0 s before the burst peak time. Although the 356 Hz signal is also seen in 0.5–12 keV in 4 s search interval window it does not achieve statistical significance requisite for initial selection criteria. In the case of burst 3, a tentative oscillation at 367 Hz is seen in 0.5–6 keV band with an rms amplitude of about $16\% \pm 2\%$. The signal reaches a maximum power of 23 at 4.3 ± 2.0 s before the burst peak time. In the case of burst 10, a potential candidate oscillation is detected at 359 Hz in the 6–12 keV band in both 2 s and 4 s search interval windows. The oscillation seems to reach a maximum Z^2 of just over 27 at 1.3 ± 1.0 s before the burst peak time. The rms amplitude of the signal computed within the search time interval is $64\% \pm 11\%$.

To investigate the temporal behavior of the oscillations seen immediately before the bursts, we divided the light curve from 100 s (30 s for burst 10) before the burst

to the end into 1 s (or 2 s for burst 3) time intervals and determine fractional rms amplitudes of the oscillation signal for each interval. Results for bursts 1, 3, and 10 are presented in Figure 7, where, in the upper panels, we show the time dependent variation of the rms amplitudes determined in each interval and also the light curves in the energy range where the oscillation is observed. It is clearly seen that the rms amplitudes are high in the intervals where the power is maximum and then decrease as the burst rises. Similar to the fractional rms amplitude evolutions seen here, Chakraborty & Bhattacharyya (2014) reported that burst oscillations detected during the rises of the bursts show a decreasing trend of fractional rms amplitude with time. They infer a typical timescale for the oscillations to be undetectable as 2.5 s and attribute this time to the flame spreading. However, in the case of the oscillations reported here, the decrease in the rms amplitude happens instantaneously instead of showing a similar decreasing trend. Lower panels of Figure 7 show pulse profiles obtained by folding the interval with the oscillation frequency where the measured rms is high (red curve) and at peak of the burst interval (blue curve).

3.2.1. Monte Carlo simulations

In order to assess the significance of the candidate oscillations observed during the X-ray bursts, we followed two different methods. As an initial step, we generated 10^5 simulations of the null hypothesis (no oscillations) for each of the eight bursts including the entire time window we initially looked for. We randomized the arrival times of events in each time window (2s or 4s) and also allowed for variation of the observed count rates assuming a Poisson distribution. We followed exactly the same procedures for the timing analysis of simulated burst profiles for each burst and evaluated how frequently a maximum Z^2 value equal to or greater than the observed value in the real data is obtained in the simulated data. The resulting maximum Z^2 values are distributed almost homogeneously around the burst times although there is a minor trend following the count rate, especially in the 6–12 keV band. We determined the p-value from the distribution of simulated maximum Z^2 values for each burst and transformed them to σ -values to establish their significance. We found from the simulation that six out of eight bursts show significances between 2.5 – 3.2σ while two bursts are insignificant ($\leq 2.1\sigma$). This further supports the conclusion that these six bursts have real signals. This study presents the discovery of oscillations in bursts 1, 10, and 11 for the first time, whereas oscillations observed during bursts 4, 7 and 8 have already been reported by Mahmoodifar et al. (2019).

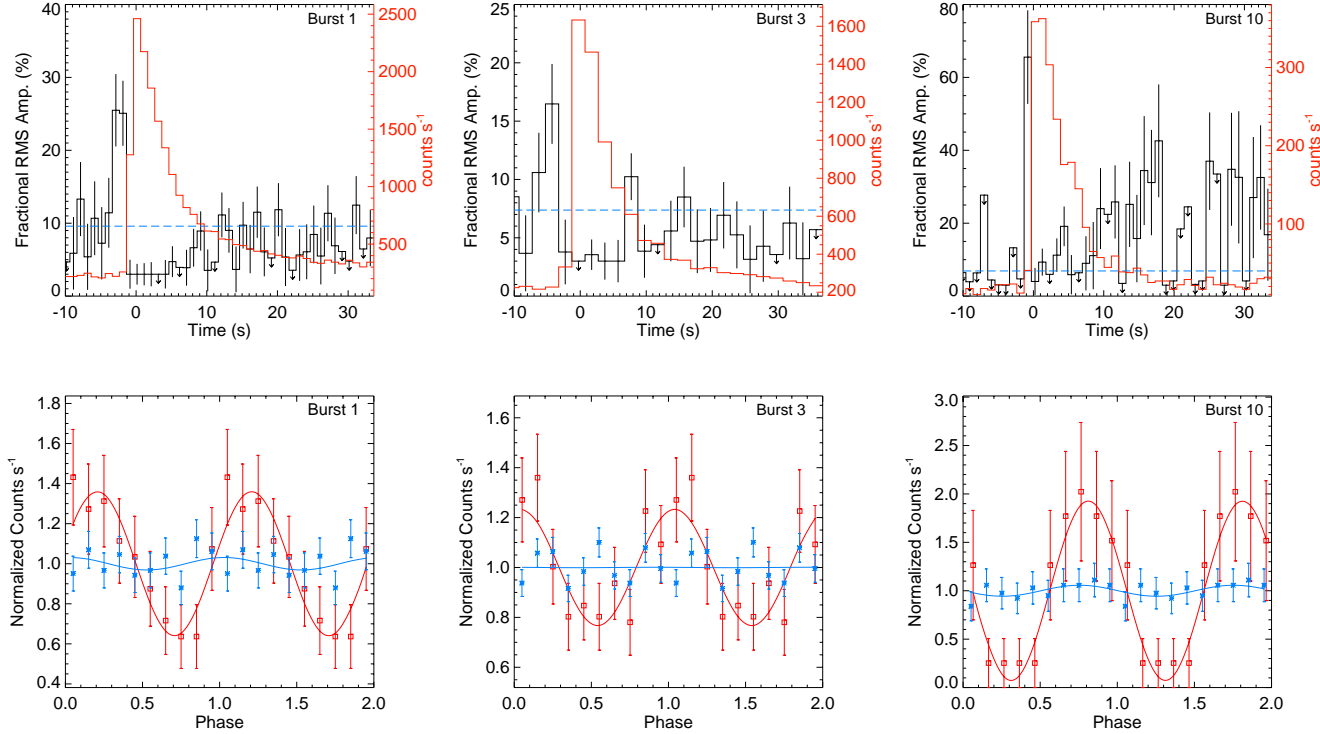


Figure 7. *Upper Panel:* Under the assumption that there are oscillations at 356.1 Hz, 367.0 Hz and 359.0 Hz, the evolution of the fractional rms amplitudes (black lines) together with the burst light curves (red lines) in the 0.5–12, 0.5–6, and 6–12 keV for bursts 1, 3, and 10 (from left to right panels), respectively. Amplitudes are calculated in 1 s intervals for bursts 1 and 10 and in 2 s intervals for burst 3. Arrows indicate upper limits. The amplitudes are high in two bins (2 or 4 s for burst 1 and 3) just before burst onset, then drop below the detection level during the burst peak. The horizontal blue dashed lines show the average rms amplitude values calculated using the 100 s interval before the onset for bursts 1 and 3, and 30 s interval before the onset for burst 10. *Lower Panel:* Phase-folded light curves (squares and stars with the error bars) obtained by folding 1 s intervals for bursts 1 and 10, and 2 s intervals for burst 3. The best-fitting sinusoidal model (solid lines) for the bins just before the onset (red) and the peak (blue) are also shown. Phase-folded light curves were normalized by constant values from the best-fitting sinusoidal models, for clarity.

For bursts 1 and 10 showing oscillations prior to the burst, we found 301 and 662 cases out of 10^5 simulations, where the maximum Z^2 is greater than the value we report, indicating 3σ and 2.7σ significance, respectively. We note that 30 and 61 cases ($\simeq 10\%$) out of them are seen prior to simulated bursts for bursts 1 and 10, respectively. However, we found 3592 cases with the maximum Z^2 greater than the reported value for burst 3. This shows that the oscillation seen prior to burst 3 is not significant enough, with only 2.1σ .

In Figure 8, we only present resulting contour maps together with light curves of bursts 1, 10 and 11 since the remaining three bursts have been reported previously in Mahmoodifar et al. (2019). Power spectra are reconstructed using windows being shifted by 0.25 s and contours are plotted for Z_1^2 values of 10 and 15 to the maximum value, in steps of 2, in blue and red, respectively. We adjusted the frequency range in the figure according to the frequency of the significant signal. The

lower panels in Figure 8 show phase-folded light curves calculated in the search interval window and in the energy band in which the signal with maximum power is identified.

As another method to check the chance occurrence of the oscillatory signals prior to the bursts we also performed the same timing analysis procedures (but time windows being shifted by 0.25 s) for all 73 *NICER* observations of 4U 1728–34, only excluding the burst times, already used to search for burst oscillations in Subsection 3.2. In Figure 9 we present histograms of maximum Z^2 values from the total 656,685 and 659,792 time steps of 2 s and 4 s time windows, respectively, in the three energy bands. First of all, we could not find any time interval within the existing clean event files of the analyzed observations here where the Z^2 is systematically larger for a time interval longer than the size of the search window (2 or 4 seconds). This indicates that no intermittent pulsation or oscillation behaviour is observed from

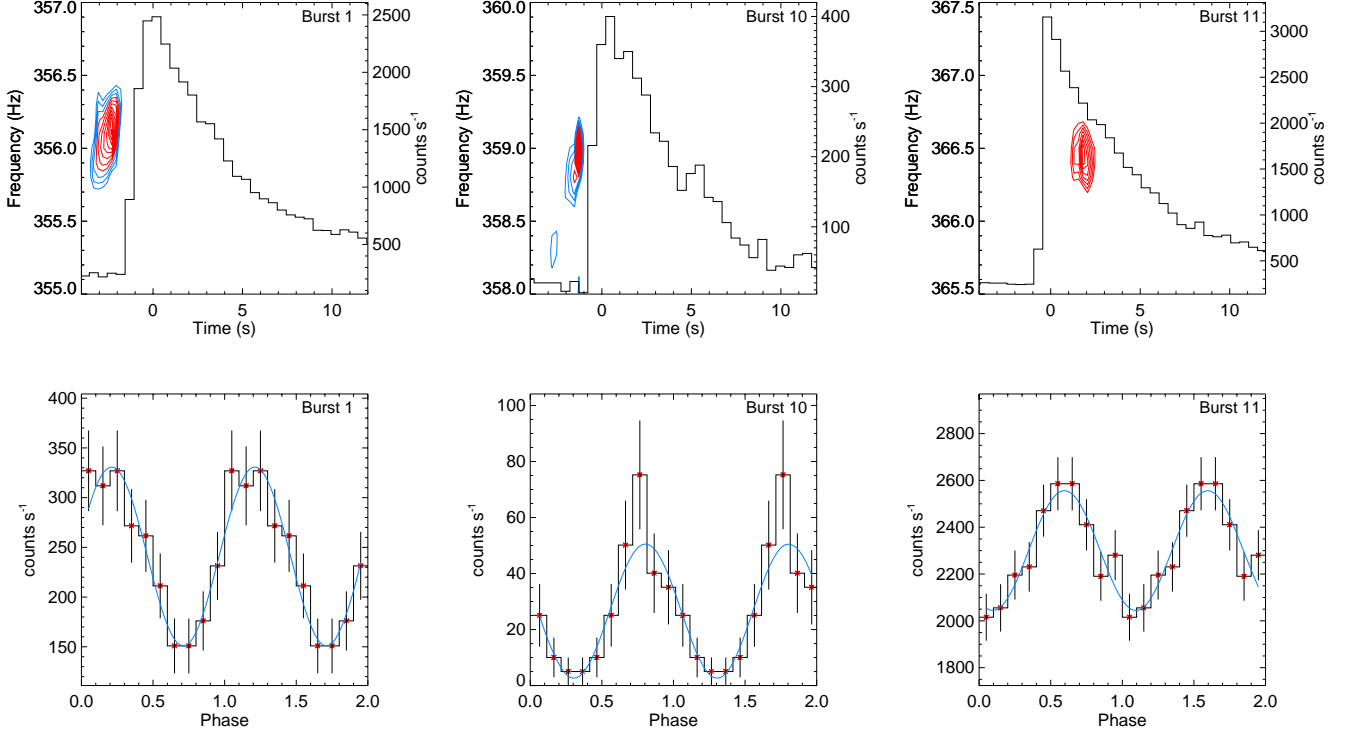


Figure 8. *Upper Panels:* Light curves of the X-ray bursts with a bin size of 0.5 s (black), where we modified the time axis of the plots to begin at the peak and contours of dynamical power spectra showing burst oscillations for bursts 1, 10 and 11 from 4U 1728–34 (from left to right). Contours refer to $Z^2 \geq 10$ (blue) and ≥ 15 (red) up to the maximum with steps of 2. *Lower Panels:* Pulse profiles calculated using the 2 s interval together with the best-fitting sinusoidal model (blue line).

4U 1728–34 within any of the *NICER* observations in the 355–370 Hz range.

The analysis of non-bursting times across all observations revealed that the chance probability of obtaining Z^2 values as high as 30.5 and 27.6 (detected in the 0.5–12 and 6–12 keV bands, respectively, similar to bursts 1 and 10) was remarkably low, at 0.0026% (17 cases) and 0.0023% (15 cases). We note that for the burst 3 the same probability is found to be 0.12% (817 cases). This test also supports the conclusion that the detection significance of the oscillations are highly unlikely to be obtained by chance and likely related to bursts 1 and 10.

3.2.2. The origin of the pulsations before bursts 1 and 10

To the best of our knowledge this is the first time from any bursting low mass X-ray binary that burst oscillations are detected just prior to bursts and end with their rise. We must here note that usually an increase in the X-ray count rate is taken as an indication that the burst has started, but most likely the thermonuclear runaway starts before the observed rise as there should be a finite time for the heat/radiation to diffuse from the burning layer depth to the photosphere. This time difference likely depends on the ignition depth and the dominating

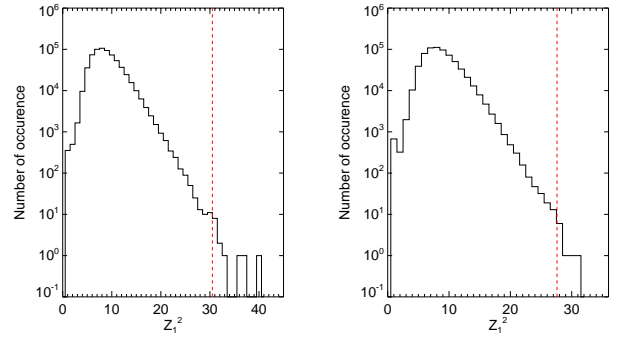


Figure 9. Distribution of maximum Z^2 values obtained from whole 73 *NICER* observations of 4U 1728–34, in the energy range of 0.5–12 keV (left), and 6–12 keV (right). The red dashed lines show the maximum Z^2 values measured from the oscillations prior to the bursts in the related energy band.

transport mechanism (dependent, in turn, on composition and accretion rate; see, e.g., Woosley et al. 2004; Fisker et al. 2008; José et al. 2010, and Cumming & Bildsten 2000 for analytical estimates). We looked for any statistically significant deviation in the observed count rate when the oscillations are detected compared to the

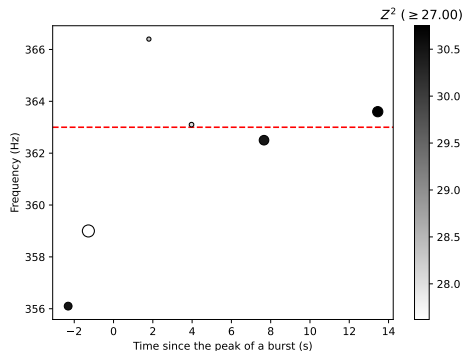


Figure 10. Frequencies of the detected oscillations as a function of time since the peak of a burst. Only the oscillations which were selected in Subsection 3.2.1 are shown. Red dashed line shows the 363 Hz level. The color scale shows Z^2 values, while the size of the symbols changes with increasing fractional rms amplitude

source count rates before. Unfortunately we could not obtain any significant deviation.

To examine potential frequency evolution of the oscillations, in Figure 8 we lowered our limit on the Z^2 to 10 and showed in blue some additional contours. Although such a low Z^2 value is not statistically significant these additional contours show that in both cases there may be an increase in the oscillation frequency by about 0.5–1 Hz within about one and two seconds prior to the bursts in bursts 1 and 10, respectively.

Frequency drifts in burst oscillation detections have been observed in various sources (Muno et al. 2002a; Watts 2012). Often as a burst progresses, the detected oscillation frequency drifts upwards by a few Hz (Watts 2012). A notable instance involves Wijnands et al. (2001), who reported a 5 Hz frequency drift during a burst from the X-ray binary X1658–298. A similar, upward drift is also observed here in burst 4, where the frequency increases by 5 Hz, although the oscillations are detected at different energy bands and with varying significances (as in the case of Wijnands et al. (2001); see Table 4). The oscillations detected here are not strong enough to be followed individually in terms of frequency drifts. However, we plot the frequencies of all the significant oscillations as a function of the time they are detected before or after the peak in Figure 10, where the asymptotic drift towards 363 Hz can be seen especially when considering the oscillations detected prior to the bursts. This suggests that the nature of these oscillations may be similar to what is observed during the bursts. Based on all these findings we now discuss possible origins for our detections.

One plausible explanation for the oscillations before the rise is related to a hot spot and its time evolution. For this scenario to work, the initial burst rise may have a weak, slowly increasing part, that is not significant enough to discern in the count rate, but might be showing up as pulsations. This is partly at odds with the expectation that hydrogen-poor bursts would manifest relatively quickly after ignition (Woodsley et al. 2004; Cumming & Bildsten 2000), but it could be related to multi-D effects such as confinement or finite time flame spreading. As shown by Spitkovsky et al. (2002) and Cavecchi & Spitkovsky (2019) such a flame can then quickly cover the surface of the neutron star causing the disappearance of the detected oscillations. A hot spot would be more justified by an off-equator ignition and this is more likely for slow rotators such as 4U 1728–34 (Spitkovsky et al. 2002). Furthermore, Cooper & Narayan (2007) and Cavecchi et al. (2020) suggest that as the mass accretion rate increases the ignition latitude may also rise, due to the fact that burning on the equator should approach stability, which fits nicely with the fact that the rms of the detections before the bursts increases with the persistent count rate (as a proxy to the accretion rate; see Table 1 and Table 4), since ignition at the equator should lead quickly to a ring around the star, more than a hot spot. However, in such a case one would expect to see similar oscillations associated to bursts 2, 9 and 11 as these bursts seem to be happening at similar persistent fluxes. We note that these bursts are labelled as possible photospheric radius expansion events and, unlike bursts 1 and 10, not clear PREs, and this may have some bearing on the fact that we do or do not see any pulsation, although in general PREs weaken the pulsations near the peak. Regarding the hot spot propagation scenario it is worth highlighting that, given the time between the start of the bursts and the detection of the oscillations and using the speed for flame spread from simulations (Cavecchi & Spitkovsky 2019) we find that for burst 1 and burst 10 the flame spread reaches 5.6 and 2.8 km, respectively.

Another effect may be that the energy input from the thermonuclear burning excites oscillation modes (such as r-modes, initially proposed as an explanation for burst oscillations by Heyl 2004, see also Strohmayer & Lee 1996), which could influence the surface emission pattern. However, we note that these modes take some time to grow, and they are global waves on the star, so one would expect that the burning flame should have expanded significantly in order to put enough energy into them (and are indeed expected more during the tail of the bursts; see Heyl 2004 and also Chambers & Watts 2020). Other related mode instabilities, such as

the shear instabilities proposed by Cumming (2005), are similar and also only suitable to explain pulsations in the tails.

A final speculation may be related to accretion powered pulsations (APPs) as also suggested by Mahmoodifar et al. (2019) for oscillations observed in the tails of bursts 4 and 8 with a large fractional rms amplitude. Using RXTE observations of HETE J1900.1–2455, Galloway et al. (2007) reported that APPs are influenced by the bursts. They reported an increase in the amplitude more or less in coincidence with some bursts and then a decline afterwards. On the other hand, Patruno et al. (2009) reported similar findings from SAX J1748.9–2021, but concluded that there is not a clear trend, noting that some bursts appeared to strengthen the APPs and others did not. In both of these sources persistent or intermittent pulsations have been observed clearly. In the case of 4U 1728–34 no such pulsation has been reported before and our search for all the non-bursting times in the *NICER* data revealed no such significant pulsation. One explanation could be that 4U 1728–34 has extremely weak APPs, if any at all, and that the oscillations reported here are APPs which are enhanced by the burning/burst occurrence, similar to what Mahmoodifar et al. (2019) suggested for the burst oscillations in the tail of bursts 4 and 8. The fact that we detect oscillations before the start of the bursts perhaps makes these detections more suggestive of that phenomenology. If this is the explanation, than the detections reported here are not the first burst oscillations detected before a burst, but perhaps the first APPs from 4U 1728–34.

4. CONCLUSIONS

We have searched two years of archival *NICER* data of the low mass X-ray binary, 4U 1728–34. We detected 11 X-ray bursts, 3 of which show photospheric radius expansion. Our results show that, unlike some of the earlier results from *NICER*, the use of a scaling factor is statistically not required to model the X-ray spectra extracted during the bursts. This result is most likely due to the significantly large hydrogen column density value in the line of sight towards 4U 1728–34. Similar results are obtained for 4U 1608–52 and XTE 1739–286 (Bult et al. 2021; Güver et al. 2021) for which the absorption due to interstellar medium is similarly large. We compared our spectral results at the peak times of each burst to the extensive MINBAR sample. The results seem to agree with earlier measurements in terms of peak flux and blackbody parameters. Similarly, Güver et al. (2022a) compared the spectral parameters at the peaks of the bursts observed from Aql X-1 with the MIN-

BAR sample and showed that when the f_a method is not employed, the inferred parameters show a systematic trend of being lower than what is inferred from the MINBAR sample, which is based on data obtained in the 3–25 keV band. The fact that we do not see such a systematic trend here, as well as the much better fits compared to the results from other sources (Güver et al. 2022a,b), together with the N_H , further imply that the excess observed in some of the bursters is probably only limited to the soft X-ray band (below 2.5 keV). This is similar to the findings by Güver et al. (2022a), where fitting only the 3–10 keV data without an f_a factor resulted in similar spectral parameters for the bursts when using the full band of the *NICER* but using the f_a factor.

We also reported our search for burst oscillations during the 11 bursts detected. In 6 of these 11 events, we detected significant oscillations at around 363 Hz, similar to previous reports from this source (see, e.g., Strohmayer et al. 1996; Mahmoodifar et al. 2019; Galloway et al. 2020). We found that two bursts featured oscillations between their peak and e-folding time, while another two displayed oscillations during burst tails. Although, previous reports of burst oscillations from 4U 1728–34 were confined to the 363 ± 5 Hz interval we here focused on a broader frequency range. Such an analysis enabled us to detect several similarly significant signals below or above the previous frequency limits.

Most remarkably, in two bursts we detect significant oscillations just preceding the observed X-ray bursts. To the best of our knowledge this is the first time from any bursting low mass X-ray binary that burst oscillations are detected just prior to bursts and end with their rise. In burst 1 we detect oscillations prior to the burst in the 0.5–12 keV ($Z^2 = 30.5$) and 0.5–6 keV ($Z^2 = 27$) bands, while they are absent in the 6–12 keV range ($Z^2 < 15$). On the other hand in burst 10 while the oscillations are detected in the 6–12 keV band ($Z^2 = 27.6$) they are not detected at lower energies. The difference may at least be partly related to the observed number of counts in each case, since during burst 10 the source is brighter by about 15%. Given the strong interstellar absorption towards the source which compensates for the large effective area of *NICER* at lower energies it would be expected that such oscillations may be detected in the archival Rossi X-ray Timing Explorer (RXTE) data. Finding more examples of oscillations outside the bursts of 4U 1728–34 will certainly help understanding their nature and their connections to the thermonuclear burning. A separate analysis on the search for similar events

in the RXTE archive is currently underway and will be presented elsewhere.

ACKNOWLEDGEMENTS

We thank the referee for valuable comments and suggestions that improved the manuscript. This work is supported by the Scientific Research Projects Coordination Unit of Istanbul University (ADEP Project No: FBA-2023-39409) and the Turkish Republic, Presidency

of Strategy and Budget project, 2016K121370. YC acknowledges support from the grant RYC2021-032718-I, financed by MCIN/AEI/10.13039/501100011033 and the European Union NextGenerationEU/PRTR. This work was supported by NASA through the *NICER* mission and the Astrophysics Explorers Program.

DATA AVAILABILITY

All the data used in this publication is publicly available through NASA/HEASARC archives.

REFERENCES

- Astropy Collaboration, Price-Whelan, A. M., Sipőcz, B. M., et al. 2018, *AJ*, 156, 123, doi: [10.3847/1538-3881/aabc4f](https://doi.org/10.3847/1538-3881/aabc4f)
- Basinska, E. M., Lewin, W. H. G., Sztajno, M., Cominsky, L. R., & Marshall, F. J. 1984a, *ApJ*, 281, 337, doi: [10.1086/162103](https://doi.org/10.1086/162103)
- . 1984b, *ApJ*, 281, 337, doi: [10.1086/162103](https://doi.org/10.1086/162103)
- Bhattacharyya, S. 2010, *Advances in Space Research*, 45, 949, doi: [10.1016/j.asr.2010.01.010](https://doi.org/10.1016/j.asr.2010.01.010)
- Bhattacharyya, S., Yadav, J. S., Sridhar, N., et al. 2018, *ApJ*, 860, 88, doi: [10.3847/1538-4357/aac495](https://doi.org/10.3847/1538-4357/aac495)
- Bilous, A. V., & Watts, A. L. 2019, *ApJS*, 245, 19, doi: [10.3847/1538-4365/ab2fe1](https://doi.org/10.3847/1538-4365/ab2fe1)
- Bogdanov, S., Lamb, F. K., Mahmoodifar, S., et al. 2019, *ApJL*, 887, L26, doi: [10.3847/2041-8213/ab5968](https://doi.org/10.3847/2041-8213/ab5968)
- Buccheri, R., Bennett, K., Bignami, G. F., et al. 1983, *A&A*, 128, 245
- Buisson, D. J. K., Altamirano, D., Bult, P., et al. 2020, *MNRAS*, 499, 793, doi: [10.1093/mnras/staa2749](https://doi.org/10.1093/mnras/staa2749)
- Bult, P., Jaisawal, G. K., Güver, T., et al. 2019, *ApJL*, 885, L1, doi: [10.3847/2041-8213/ab4ae1](https://doi.org/10.3847/2041-8213/ab4ae1)
- Bult, P., Altamirano, D., Arzoumanian, Z., et al. 2021, *ApJ*, 907, 79, doi: [10.3847/1538-4357/abd54b](https://doi.org/10.3847/1538-4357/abd54b)
- Bult, P., Mancuso, G. C., Strohmayer, T. E., et al. 2022, *ApJ*, 940, 81, doi: [10.3847/1538-4357/ac9b26](https://doi.org/10.3847/1538-4357/ac9b26)
- Cavecchi, Y., Galloway, D. K., Goodwin, A. J., Johnston, Z., & Heger, A. 2020, *MNRAS*, 499, 2148, doi: [10.1093/mnras/staa2858](https://doi.org/10.1093/mnras/staa2858)
- Cavecchi, Y., & Spitkovsky, A. 2019, *ApJ*, 882, 142, doi: [10.3847/1538-4357/ab3650](https://doi.org/10.3847/1538-4357/ab3650)
- Chakrabarty, D., Morgan, E. H., Munro, M. P., et al. 2003, *Nature*, 424, 42, doi: [10.1038/nature01732](https://doi.org/10.1038/nature01732)
- Chakraborty, M., & Bhattacharyya, S. 2014, *ApJ*, 792, 4, doi: [10.1088/0004-637X/792/1/4](https://doi.org/10.1088/0004-637X/792/1/4)
- Chambers, F. R. N., & Watts, A. L. 2020, *MNRAS*, 491, 6032, doi: [10.1093/mnras/stz3449](https://doi.org/10.1093/mnras/stz3449)
- Cooper, R. L., & Narayan, R. 2007, *ApJL*, 657, L29, doi: [10.1086/513077](https://doi.org/10.1086/513077)
- Cumming, A. 2005, *ApJ*, 630, 441, doi: [10.1086/431731](https://doi.org/10.1086/431731)
- Cumming, A., & Bildsten, L. 2000, *ApJ*, 544, 453, doi: [10.1086/317191](https://doi.org/10.1086/317191)
- D’Aí, A., di Salvo, T., Iaria, R., et al. 2006, *A&A*, 448, 817, doi: [10.1051/0004-6361:20053228](https://doi.org/10.1051/0004-6361:20053228)
- Damen, E., Magnier, E., Lewin, W. H. G., et al. 1990, *A&A*, 237, 103
- Di Salvo, T., Iaria, R., Burderi, L., & Robba, N. R. 2000, *ApJ*, 542, 1034, doi: [10.1086/317029](https://doi.org/10.1086/317029)
- Egron, E., di Salvo, T., Burderi, L., et al. 2011, *A&A*, 530, A99, doi: [10.1051/0004-6361/201016093](https://doi.org/10.1051/0004-6361/201016093)
- Fisker, J. L., Schatz, H., & Thielemann, F.-K. 2008, *ApJS*, 174, 261, doi: [10.1086/521104](https://doi.org/10.1086/521104)
- Fragile, P. C., Ballantyne, D. R., & Blankenship, A. 2020, *Nature Astronomy*, 4, 541, doi: [10.1038/s41550-019-0987-5](https://doi.org/10.1038/s41550-019-0987-5)
- Fragile, P. C., Ballantyne, D. R., Maccarone, T. J., & Witry, J. W. L. 2018, *ApJL*, 867, L28, doi: [10.3847/2041-8213/aaeb99](https://doi.org/10.3847/2041-8213/aaeb99)
- Franco, L. M. 2001, *ApJ*, 554, 340, doi: [10.1086/321341](https://doi.org/10.1086/321341)
- Freeman, P., Doe, S., & Siemiginowska, A. 2001, in *Society of Photo-Optical Instrumentation Engineers (SPIE) Conference Series*, Vol. 4477, *Astronomical Data Analysis*, ed. J.-L. Starck & F. D. Murtagh, 76–87, doi: [10.1117/12.447161](https://doi.org/10.1117/12.447161)
- Galloway, D. K., Morgan, E. H., Krauss, M. I., Kaaret, P., & Chakrabarty, D. 2007, *ApJL*, 654, L73, doi: [10.1086/510741](https://doi.org/10.1086/510741)
- Galloway, D. K., Munro, M. P., Hartman, J. M., Psaltis, D., & Chakrabarty, D. 2008, *ApJS*, 179, 360, doi: [10.1086/592044](https://doi.org/10.1086/592044)
- Galloway, D. K., Psaltis, D., Chakrabarty, D., & Munro, M. P. 2003, *ApJ*, 590, 999, doi: [10.1086/375049](https://doi.org/10.1086/375049)
- Galloway, D. K., in’t Zand, J., Chenevez, J., et al. 2020, *ApJS*, 249, 32, doi: [10.3847/1538-4365/ab9f2e](https://doi.org/10.3847/1538-4365/ab9f2e)

- Gendreau, K. C., Arzoumanian, Z., Adkins, P. W., et al. 2016, in *Society of Photo-Optical Instrumentation Engineers (SPIE) Conference Series*, Vol. 9905, *Space Telescopes and Instrumentation 2016: Ultraviolet to Gamma Ray*, ed. J.-W. A. den Herder, T. Takahashi, & M. Bautz, 99051H, doi: [10.1117/12.2231304](https://doi.org/10.1117/12.2231304)
- Güver, T., Özel, F., & Psaltis, D. 2012a, *ApJ*, 747, 77, doi: [10.1088/0004-637X/747/1/77](https://doi.org/10.1088/0004-637X/747/1/77)
- Güver, T., Psaltis, D., & Özel, F. 2012b, *ApJ*, 747, 76, doi: [10.1088/0004-637X/747/1/76](https://doi.org/10.1088/0004-637X/747/1/76)
- Güver, T., Boztepe, T., Göğüş, E., et al. 2021, *ApJ*, 910, 37, doi: [10.3847/1538-4357/abe1ae](https://doi.org/10.3847/1538-4357/abe1ae)
- Güver, T., Boztepe, T., Ballantyne, D. R., et al. 2022a, *MNRAS*, 510, 1577, doi: [10.1093/mnras/stab3422](https://doi.org/10.1093/mnras/stab3422)
- Güver, T., Bostancı, Z. F., Boztepe, T., et al. 2022b, *ApJ*, 935, 154, doi: [10.3847/1538-4357/ac8106](https://doi.org/10.3847/1538-4357/ac8106)
- Hansen, C. J., & van Horn, H. M. 1975, *ApJ*, 195, 735, doi: [10.1086/153375](https://doi.org/10.1086/153375)
- Hasinger, G., & van der Klis, M. 1989, *A&A*, 225, 79
- Heyl, J. S. 2004, *ApJ*, 600, 939, doi: [10.1086/379966](https://doi.org/10.1086/379966)
- Hoffman, J. A., Lewin, W. H. G., Doty, J., et al. 1976, *ApJL*, 210, L13, doi: [10.1086/182292](https://doi.org/10.1086/182292)
- Hunter, J. D. 2007, *Computing in Science & Engineering*, 9, 90, doi: [10.1109/MCSE.2007.55](https://doi.org/10.1109/MCSE.2007.55)
- José, J., Moreno, F., Parikh, A., & Iliadis, C. 2010, *ApJS*, 189, 204, doi: [10.1088/0067-0049/189/1/204](https://doi.org/10.1088/0067-0049/189/1/204)
- Kajava, J. J. E., Sánchez-Fernández, C., Kuulkers, E., & Poutanen, J. 2017, *A&A*, 599, A89, doi: [10.1051/0004-6361/201629542](https://doi.org/10.1051/0004-6361/201629542)
- Keek, L., Arzoumanian, Z., Bult, P., et al. 2018a, *ApJL*, 855, L4, doi: [10.3847/2041-8213/aab104](https://doi.org/10.3847/2041-8213/aab104)
- Keek, L., Arzoumanian, Z., Chakrabarty, D., et al. 2018b, *ApJL*, 856, L37, doi: [10.3847/2041-8213/aab904](https://doi.org/10.3847/2041-8213/aab904)
- Kellogg, E., Gursky, H., Murray, S., Tananbaum, H., & Giacconi, R. 1971, *ApJL*, 169, L99, doi: [10.1086/180820](https://doi.org/10.1086/180820)
- Kuulkers, E., den Hartog, P. R., in't Zand, J. J. M., et al. 2003, *A&A*, 399, 663, doi: [10.1051/0004-6361:20021781](https://doi.org/10.1051/0004-6361:20021781)
- Lamb, D. Q., & Lamb, F. K. 1978, *ApJ*, 220, 291, doi: [10.1086/155905](https://doi.org/10.1086/155905)
- Lewin, W. H. G., Clark, G., & Doty, J. 1976, *IAUC*, 2922, 1
- Mahmoodifar, S., Strohmayer, T. E., Bult, P., et al. 2019, *ApJ*, 878, 145, doi: [10.3847/1538-4357/ab20c4](https://doi.org/10.3847/1538-4357/ab20c4)
- Mondal, A. S., Pahari, M., Dewangan, G. C., Misra, R., & Raychaudhuri, B. 2017, *MNRAS*, 466, 4991, doi: [10.1093/mnras/stx039](https://doi.org/10.1093/mnras/stx039)
- Muno, M. P., Chakrabarty, D., Galloway, D. K., & Psaltis, D. 2002a, *ApJ*, 580, 1048, doi: [10.1086/343793](https://doi.org/10.1086/343793)
- Muno, M. P., Özel, F., & Chakrabarty, D. 2002b, *ApJ*, 581, 550, doi: [10.1086/344152](https://doi.org/10.1086/344152)
- Okajima, T., Soong, Y., Balsamo, E. R., et al. 2016, in *Society of Photo-Optical Instrumentation Engineers (SPIE) Conference Series*, Vol. 9905, *Space Telescopes and Instrumentation 2016: Ultraviolet to Gamma Ray*, ed. J.-W. A. den Herder, T. Takahashi, & M. Bautz, 99054X, doi: [10.1117/12.2234436](https://doi.org/10.1117/12.2234436)
- Özel, F., & Freire, P. 2016, *ARA&A*, 54, 401, doi: [10.1146/annurev-astro-081915-023322](https://doi.org/10.1146/annurev-astro-081915-023322)
- Özel, F., Psaltis, D., Güver, T., et al. 2016, *ApJ*, 820, 28, doi: [10.3847/0004-637X/820/1/28](https://doi.org/10.3847/0004-637X/820/1/28)
- Patruno, A., Altamirano, D., Hessels, J. W. T., et al. 2009, *ApJ*, 690, 1856, doi: [10.1088/0004-637X/690/2/1856](https://doi.org/10.1088/0004-637X/690/2/1856)
- Qiao, E., & Liu, B. F. 2019, *MNRAS*, 487, 1626, doi: [10.1093/mnras/stz1365](https://doi.org/10.1093/mnras/stz1365)
- Remillard, R. A., Loewenstein, M., Steiner, J. F., et al. 2022, *AJ*, 163, 130, doi: [10.3847/1538-3881/ac4ae6](https://doi.org/10.3847/1538-3881/ac4ae6)
- Shaposhnikov, N., Titarchuk, L., & Haberl, F. 2003, *ApJL*, 593, L35, doi: [10.1086/378255](https://doi.org/10.1086/378255)
- Sleator, C. C., Tomsick, J. A., King, A. L., et al. 2016, *ApJ*, 827, 134, doi: [10.3847/0004-637X/827/2/134](https://doi.org/10.3847/0004-637X/827/2/134)
- Speicher, J., Ballantyne, D. R., & Fragile, P. C. 2022, *MNRAS*, 509, 1736, doi: [10.1093/mnras/stab3087](https://doi.org/10.1093/mnras/stab3087)
- Spitkovsky, A., Levin, Y., & Ushomirsky, G. 2002, *ApJ*, 566, 1018, doi: [10.1086/338040](https://doi.org/10.1086/338040)
- Strohmayer, T., & Bildsten, L. 2006, *New views of thermonuclear bursts*, Cambridge Astrophysics (Cambridge University Press), 113–156, doi: [10.1017/CBO9780511536281.004](https://doi.org/10.1017/CBO9780511536281.004)
- Strohmayer, T. E., & Lee, U. 1996, *ApJ*, 467, 773, doi: [10.1086/177651](https://doi.org/10.1086/177651)
- Strohmayer, T. E., Zhang, W., & Swank, J. H. 1997, *ApJL*, 487, L77, doi: [10.1086/310880](https://doi.org/10.1086/310880)
- Strohmayer, T. E., Zhang, W., Swank, J. H., et al. 1996, *ApJL*, 469, L9, doi: [10.1086/310261](https://doi.org/10.1086/310261)
- Van Der Walt, S., Colbert, S. C., & Varoquaux, G. 2011, *Computing in Science & Engineering*, 13, 22
- van Paradijs, J. 1979, *ApJ*, 234, 609, doi: [10.1086/157535](https://doi.org/10.1086/157535)
- van Paradijs, J., Penninx, W., & Lewin, W. H. G. 1988, *MNRAS*, 233, 437, doi: [10.1093/mnras/233.2.437](https://doi.org/10.1093/mnras/233.2.437)
- van Straaten, S., van der Klis, M., Kuulkers, E., & Méndez, M. 2001, *ApJ*, 551, 907, doi: [10.1086/320234](https://doi.org/10.1086/320234)
- Verdhan Chauhan, J., Yadav, J. S., Misra, R., et al. 2017, *ApJ*, 841, 41, doi: [10.3847/1538-4357/aa6d7e](https://doi.org/10.3847/1538-4357/aa6d7e)
- Verner, D. A., & Yakovlev, D. G. 1995, *A&AS*, 109, 125
- Vincentelli, F. M., Cavecchi, Y., Casella, P., et al. 2020, *MNRAS*, 495, L37, doi: [10.1093/mnrasl/slaa049](https://doi.org/10.1093/mnrasl/slaa049)
- Vincentelli, F. M., Casella, P., Borghese, A., et al. 2023, *MNRAS*, 525, 2509, doi: [10.1093/mnras/stad2414](https://doi.org/10.1093/mnras/stad2414)
- Wang, Y., Méndez, M., Altamirano, D., et al. 2019, *MNRAS*, 484, 3004, doi: [10.1093/mnras/stz169](https://doi.org/10.1093/mnras/stz169)

- Watts, A. L. 2012, *ARA&A*, 50, 609, doi: [10.1146/annurev-astro-040312-132617](https://doi.org/10.1146/annurev-astro-040312-132617)
- Watts, A. L., Strohmayer, T. E., & Markwardt, C. B. 2005, *The Astrophysical Journal*, 634, 547, doi: [10.1086/496953](https://doi.org/10.1086/496953)
- Wes McKinney. 2010, in *Proceedings of the 9th Python in Science Conference*, ed. Stéfan van der Walt & Jarrod Millman, 56 – 61, doi: [10.25080/Majora-92bf1922-00a](https://doi.org/10.25080/Majora-92bf1922-00a)
- Wijnands, R., Strohmayer, T., & Franco, L. M. 2001, *ApJL*, 549, L71, doi: [10.1086/319128](https://doi.org/10.1086/319128)
- Wilms, J., Allen, A., & McCray, R. 2000, *ApJ*, 542, 914, doi: [10.1086/317016](https://doi.org/10.1086/317016)
- Woosley, S. E., Heger, A., Cumming, A., et al. 2004, *ApJS*, 151, 75, doi: [10.1086/381533](https://doi.org/10.1086/381533)
- Worpel, H., Galloway, D. K., & Price, D. J. 2013, *ApJ*, 772, 94, doi: [10.1088/0004-637X/772/2/94](https://doi.org/10.1088/0004-637X/772/2/94)
- . 2015, *ApJ*, 801, 60, doi: [10.1088/0004-637X/801/1/60](https://doi.org/10.1088/0004-637X/801/1/60)
- Wroblewski, P., Guver, T., & Ozel, F. 2008, arXiv e-prints, arXiv:0810.0007, doi: [10.48550/arXiv.0810.0007](https://doi.org/10.48550/arXiv.0810.0007)
- Zhang, G., Méndez, M., Zamfir, M., & Cumming, A. 2016, *MNRAS*, 455, 2004, doi: [10.1093/mnras/stv2482](https://doi.org/10.1093/mnras/stv2482)

APPENDIX

A. LIGHT CURVES OF DETECTED BURSTS

Light curves of each burst as observed in the 0.5–10 keV range are given together with the burst start, decaying e-folding and decay times. Z^2 contours are also shown in cases where a significant detection is observed.

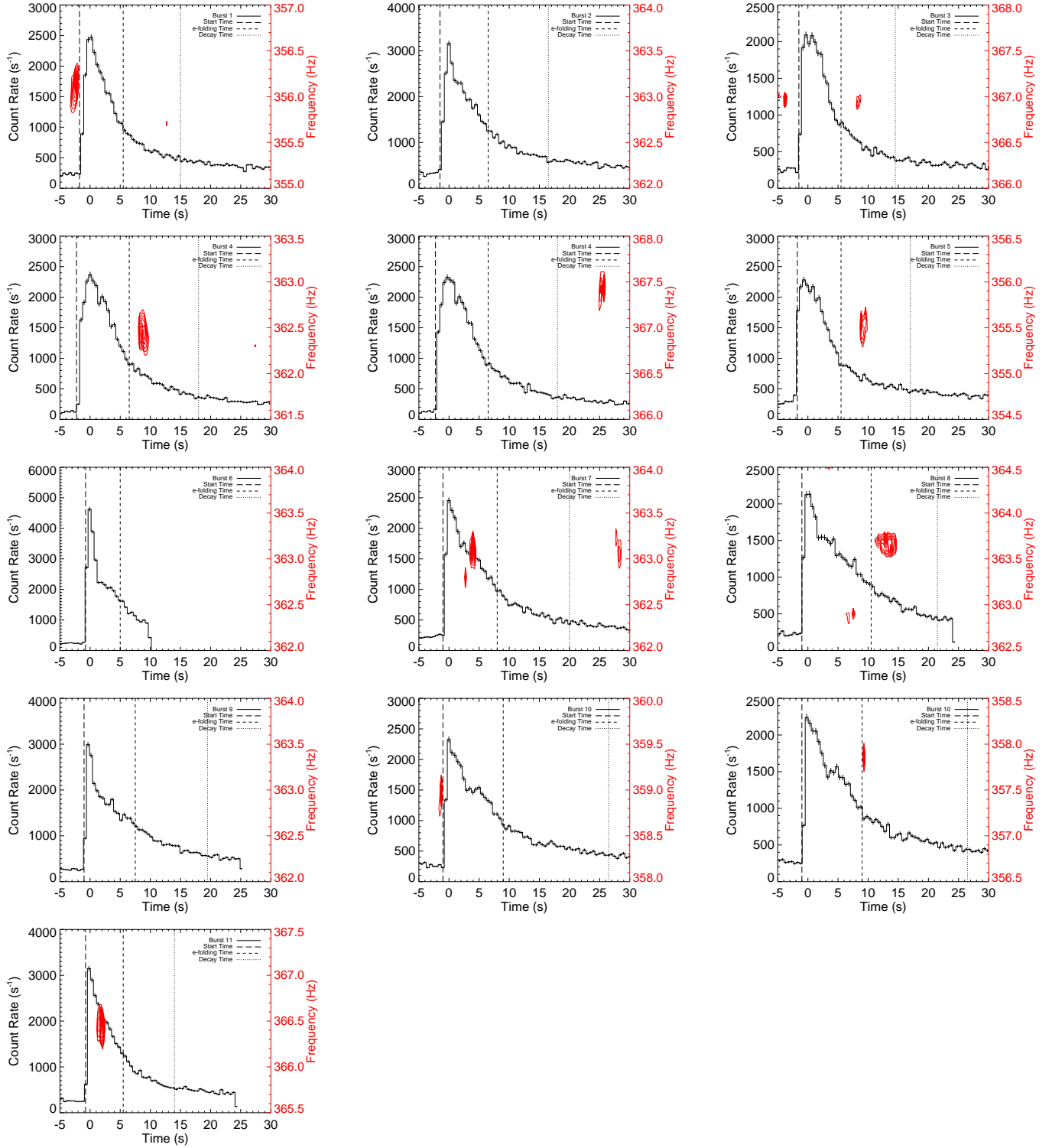


Figure A1. 0.5–10 keV light curves of detected thermonuclear X-ray bursts with contours of the candidate oscillations listed in Table 4. For bursts 4 and 10 we detect oscillations at two different frequencies, we therefore show these bursts twice. The vertical lines show the start time, the e-folding time and the decay length, defined as the time the count rate declines to 10% of the peak.